Water starvation phenomena in a segmented along the channel PEM water electrolysis cell

Niklas Hensle [a,b,*] ⓘ, Thomas Lickert [a], Nico Winterholler [a], Tom Smolinka [a], André Weber [b] ⓘ

[a] *Fraunhofer Institute for Solar Energy System ISE, Heidenhofstrasse 2, 79110, Freiburg, Germany*
[b] *Institute for Applied Materials (IAM-ET), Karlsruhe Institute of Technology (KIT), Adenauerring 20b, 76131, Karlsruhe, Germany*

HIGHLIGHTS

- Performance Analysis of a Segmented Along the Channel Cell Under Water Starvation.
- Current, Temperature, and Impedance Distribution Measurements up to 5 A·cm^{-2}
- Local Impedance Spectroscopy with Distribution of Relaxation Time analysis.
- Membrane Dry-out Leads to High Ohmic Resistance and Mostly Inactive Cell Segments.
- Mass Transport Limitations Seem not to Occur Without Significant Membrane Dry-out.

ABSTRACT

Proton exchange membrane water electrolyzers are typically operated with high water stoichiometry since the water, as a reactant, is also used as cooling agent for heat management. Water starvation phenomena are therefore not a pressing issue. However, in large industrial cell designs with challenging flow distribution, some areas of the cell may not be properly supplied with water.

This study investigates water starvation in a segmented test cell with 30 cm long flow field channels. By varying the water flow rate close to the stoichiometric level, local membrane dry-out and mass transport issues are investigated. To achieve this, the distribution of current density, temperature, and impedance are analyzed up to 5 A•cm^{-2} mean cell current density. Distribution of Relaxation Time is used to analyze the local impedance.

Our findings reveal that undersupply of water drastically affects the high frequency resistance coupled with increasing low-frequency capacitive features of the impedance, which we refer to as membrane dry-out due to mass transport limitations. However, mass transport issues, without a significant influence on membrane resistance, seem not to be relevant. By varying the gas pressure, membrane dry-out effects can be reduced which emphasizes the importance of oxygen removal at the anode.

1. Introduction

Proton exchange membrane (PEM) water electrolyzers are usually operated at high water flow rates to ensure proper water and heat management. The stoichiometric factor λ, defined as the amount of water supplied to the cell relative to the stoichiometric water consumption, typically ranges between 100 and 1000, depending on the water flow applied [1–3]. Therefore, industrial cell and stack development focuses on proper heat management to minimize temperature gradients and, subsequently, minimize stress on PEM water electrolysis cell components. A properly humidified membrane is also a key factor in cell design regarding performance and durability. Both aspects become more pressing at high current densities, which result in high water consumption and heat dissipation rates due to increased overpotentials.

At industrially relevant operation points, mass transport losses or even limitations are not relevant when using state-of-the-art flow components, such as porous transport layers (PTLs) and flow field designs, as demonstrated in our previous work where a laboratory-scaled cell designs were operated up to 25 A•cm^{-2} [4].

Despite the fact that the PEM water electrolysis industry is currently not focusing on reducing the amount of water fed to the cell and circulated in the system, investment and operating costs for pumps, ion exchangers and filters can contribute significantly to the overall costs [5–8]. External stack cooling reduces the amount of high-purity water needed and may significantly lower operating costs. Furthermore, large industrial stacks of several 1000 cm^2 active area require proper distribution of water to and within the electrolysis cells. Otherwise, partial undersupply of the active area may result in local water supply close to

---

the stoichiometric level [9–12]. These parts might significantly increase the cell's overall overpotential and accelerate degradation.

To understand such locally resolved phenomena in stacks with large active cell areas, the approach of segmented cells can provide important information. Segmentation minimizes the electrical in-plane conductivity between different cell areas and provides access to local current densities and impedance spectra. To analyze different water-to-gas ratios, cells are often segmented only along the flow field channels, referred to as *along the channel* (AtC) test cells. Typically, measurements of current density, temperature, and impedance distribution are carried out [10–15]. In this work, we use an AtC test cell with 30 cm long flow field channels and the capability to be operated at high current densities up to 10 A•cm^{-2}, as introduced earlier in Ref. [16]. The cell is divided into 10 segments along the channel, in which current density, temperature, and impedance can be measured simultaneously.

Immerz et al. investigated undersupply phenomena at current densities of up to 1.5 A•cm^{-2} in a 50 cm single-channel PEM water electrolyzer [6] and showed that operation with stoichiometries of 5 and lower leads to a drop in current density along the channel and a severe increase in mass transport resistance, as detected by locally resolved electrochemical impedance spectroscopy (EIS). They found that significant mass transport overpotentials are observable coupled with an increase in ohmic overpotentials, which indicate that an undersupply of the reactant consequently also affects membrane conductivity by drying.

Sun et al. showed in a test cell with five measurement probes along the channel that a current density drop towards the cell outlet occurs at stoichiometries <5 [12], which agrees with the findings of Immerz et al. They also observed increasing high frequency resistances (HFR) under water starvation and additionally reported increasing temperature towards the cell outlet, in combination, which indicates drying effects.

Jason K. Lee et al. analyzed gas saturation within the porous transport layer using operando neutron imaging at current densities of up to 9 A•cm^{-2} under water flow rate variation in a test cell with 0.8 cm^2 active area [17]. They report drastic gas saturation at high current densities with low water flow rates and identify a critical current density at which the high gas saturation and mass transport overpotential could lead to cell failure when exceeding this limit.

So far, all works reported on water starvation with industrially relevant cell designs and dimensions have in common that only low current densities of <2 A•cm^{-2} are investigated, which do not represent state-of-the-art or future operation points of up to 5 A•cm^{-2}.

While standard operation typically involves supplying liquid water exclusively to the anode of the cell, various unconventional water supply methods have been developed for PEM water electrolysis where water starvation phenomena are more pressing.

One notable approach, patented by Thomassen et al. [18], entails feeding process water to the cathode, requiring water permeation through the membrane for the oxygen evolution reaction (OER) at the anode. This method simplifies the system architecture by maintaining a single-phase flow on the anode side, resulting in a more compact design and reducing system costs while also minimizing risks associated with hydrogen crossover [8]. As a result, thinner membranes (<50 μm thickness) can be applied, which drastically decreases ohmic overpotentials [19]. However, challenges remain, including the necessity for precise water flow control to prevent excess water from accumulating at the anode and to avoid being forced to remove liquid water at the anode outlet. Moreover, cathode-fed cells are often operated at lower current densities compared to anode-fed cells due to potential dry-out conditions arising from mass transport limitations [20].

Another method that should be mentioned is PEM steam electrolysis. PEM steam electrolysis involves supplying water vapor instead of liquid water to the cell, which reduces the thermodynamic energy required for the electrolysis process compared to using liquid water [21]. This method benefits from faster reaction kinetics and lower operating voltages [22]. However, little work has been reported thus far, as there is still a lack of stable membrane ionomers. Water vapor can be introduced

to either the cathode or anode of the cell, with the common approach being anode feeding. Cathode feeding results in a significantly lower limiting current density compared to anode feeding and has not yet been extensively investigated [23]. The primary challenge for PEM steam electrolysis is the rapid decay of membrane performance due to elevated temperatures, which limits its investigation primarily to laboratory-scale operations [22].

In this work, we report cell performance analyses of a state-of-the-art PEM water electrolysis of up to 5 A•cm^{-2} and close to the stoichiometric level. Using current density and temperature distribution measurements, we analyze dry-out effectsof the membrane and impeded reactant supply are analyzed, which are confirmed by locally resolved EIS, with subsequent focusing on the HFR and low-frequency impedance analyses. The water flow rate is varied between 54 μl•min^{-1}•cm^{-2} and 161 μl•min^{-1}•cm^{-2}, meeting stoichiometries between $3 < \lambda < 50$ depending on the applied current density. The results are compared with industrially relevant flow rates of 10.7 ml•min^{-1}•cm^{-2}, with the cell's active area being 56 cm^2. With this work, we want to gain a deeper understanding of dry-out and mass transport effects that may occur in industrial-scaled cells or cells with unconventional cell operation.

2. Experimental

2.1. Test bench

The test bench used in this work was developed in-house at Fraunhofer ISE [21] and is designed for operation at pressures up to 50 bar, temperatures up to 80 °C, and flow rates ranging from 100 ml•min^{-1} to 2 l•min^{-1} at both the anode and cathode. The process water is circulated separately for the anode and cathode. Water-gas separators, filters, and ion exchangers provide stable conditions for the water applied and ensure a water conductivity of ≤0.1 μS•cm^{-1}. Due to electro-osmotic drag, the water level at the anode decreases while it increases at the cathode, which is balanced by a balancing line between both water tanks. Heat exchangers in the anode and cathode lines maintain stable cell temperatures with an accuracy of ±0.5 K. For operation at low water flow rates, additional electrical heat pads, which are in contact with the cell, are employed. Currents up to 1000 A can be applied using a DC (direct current) power source from TDK Lambda, Germany. For conducting EIS, Zahner Zennium X and Zahner EL1000 from Zahner Elektrik GmbH & Co. KG, Germany, are used. The test bench is controlled by in-house developed software using LabVIEW from National Instruments, USA. For full automation of the test bench, a Python-based code has been developed to interact with LabVIEW.

Since the test bench can only maintain stable water flow rates at a minimum flow of 100 ml•min^{-1}, an additional flow meter (EK-2KA-H) from Kytola Instruments, Finland, is implemented between the test cell and the original flow meter at the anode. With a bypass line, low water flow rates between 3 ml•min^{-1} (~54 μl•min^{-1}•cm^{-2} with 56 cm^2 cell area) and 9 ml•min^{-1} (161 μl•min^{-1}•cm^{-2}) can be effectively applied to the cell. During the measurements, the flow showed deviations from the mean value; therefore, we conservatively assume the accuracy to be ±1 ml•min^{-1}, which subsequently needs to be considered regarding the stoichiometry values.

2.2. Test cell design – along the channel (AtC) approach

To analyze locally resolved phenomena, we designed and built a segmented AtC cell, which is described in detail and whose functionality is discussed in our previous work [16]. Fig. 1 a) provides a schematic diagram and b) a photo of the AtC cell. The cell has an active area of 30 × 2 cm (length x width) and is segmented along the straight parallel flow field, which consists of ten milled flow field channels with 1 × 2 mm^2 (width x depth) cross-sectional area and nine 0.9 mm wide lands in between. To segment the cell, the in-plane conductivity between each segment at the anode bipolar plate and the porous transport layer (PTL)
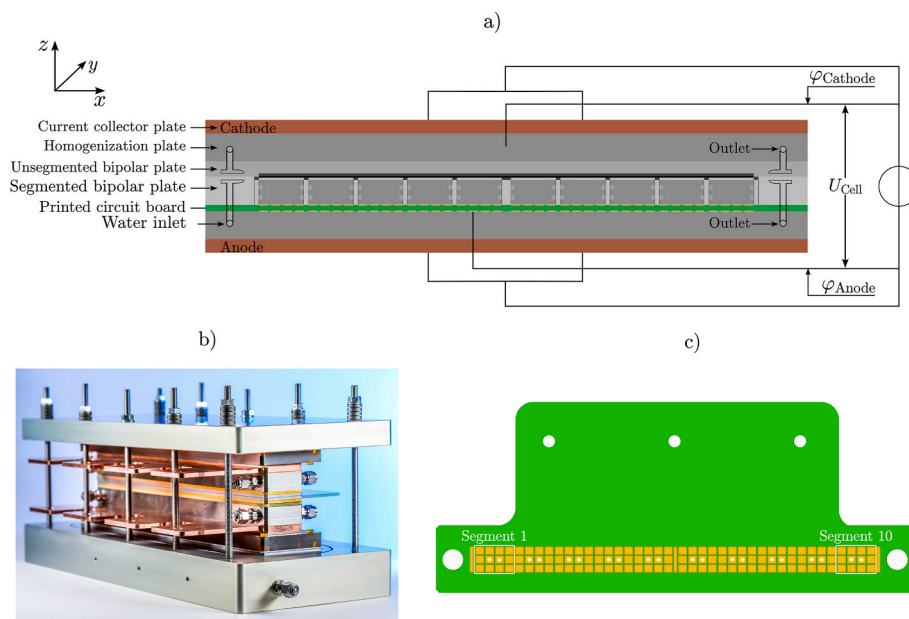
a)

b)

c)

Fig. 1. a) Simplified schematic diagram of the AtC cell, b) photo of the AtC cell, and c) design of the printed circuit board (PCB) - according to [16].

is interrupted. 10 equal segments of 2.8×2 cm^2 active area are employed along the channels, resulting in an active cell area of 56 cm^2. The anode flow field plate consists of 10 galvanically gold-coated titanium inlets, each radially sealed against a non-conductive frame. Each segment is connected to 12 measurement contacts embedded in a printed circuit board (PCB) custom-designed by DiLiCo Engineering GmbH, Germany, resulting in a total of 120 measurement points, see Fig. 1 c). The PCB is set on top of a homogenization and a current collector plate, which are not segmented. At each measurement contact, the current density and temperature are measured using a shunt resistor and Pt100 sensors, respectively. Furthermore, at the central two of the 12 contacts, a frequency response analyzer (FRA) system by Zahner Elektrik GmbH & Co. KG, Germany, is employed. With this approach, the impedance of the mean cell and in each segment can be measured in parallel. For the analysis shown here, only the mean value from all 12 contacts within one segment is considered.

The cell is designed for high current densities of 10 A•cm^{-2} (600 A absolute) and differential and balanced pressures up to 10 barg. Flow rates up to 1200 ml•min^{-1} and temperatures of 80 °C can be applied. During assembly, homogeneous compression is difficult to achieve; therefore, small variations along the segments due to different contact conditions are observed in the measurements and will be discussed. In our previous work, we demonstrated that the differences due to segment contacting have a standard deviation of less than ± 5 % of the mean current density applied. Therefore, effects along the channel can be properly analyzed, as also shown for industrially relevant cell operation in Ref. [4].

2.3. Cell components

As the catalyst-coated membrane (CCM), an E400 Gen.3 CCM by Greenerity GmbH, Germany, is used. This CCM is based on an anode IrOx and a cathode Pt/C catalyst layer printed on a Nafion®-based N115 membrane with a dry thickness of 125 μm. The catalyst loading and other structural parameters can be considered state-of-the-art for the European market, defined by *Clean Hydrogen Partnership*, European Union [24]; further information cannot be disclosed. As the anode porous transport layer (PTL), a 250 μm PTL (2GDL-10-0.25), electroplated with 200 nm of platinum on both sides, by NV Bekaert SA, Belgium, is employed. As the cathode PTL, a 215 μm thick SGL22BB by

SGL Carbon SE, Germany, is used. To ensure that no misalignment between CCM and anode and cathode PTL is present, the coated area of the CCM is equal with the sealing area.

2.4. Electrochemical measurement

All electrochemical measurements in this study are conducted at 60 °C and controlled on the anode inlet temperature of the water flow. The cell is operated normally at ambient pressure. To analyze the influence of pressure, additional operation at 3 bar$_g$ and 6 bar$_g$ balanced pressure is carried out. Water is applied only at the anode; the cathode is operated dry but humidified by the electroosmotic water drag. The water flow is varied between 54, 107 and 161 μl•min^{-1}•cm^{-2} with a referred active cell area of 56 cm^2 to analyze water starvation effects. For comparison a flow rate of 10.7 ml•min^{-1}•cm^{-2} is applied for fully hydrated conditions, as it is known for real operating conditions.

Polarization curve measurements at 0.01, 0.025, 0.05, 0.075, 0.1, 0.25, 0.5, 0.75, 1, 1.5, 2, 2.5, 3, 3.5, 4, 4.5, and 5 A•cm^{-2} are conducted with 10 min holding time each. At each current density step, the high frequency series resistance (HFR) is measured to separate ohmic and non-ohmic cell behavior. Therefore, EIS at high frequencies between 10 kHz and 100 Hz is performed. Since high frequency artifacts caused by external and internal wiring in the PCB and the test bench, the impedance at a phase angle of 0° is inaccurate for determining the HFR. We previously presented a method to extract the HFR by fitting the capacitive semicircle of the anode charge transfer process using an equivalent circuit model (ECM) consisting of a resistor in series with a RQ element (resistor with constant phase element in parallel), which is a typical approach to model charge transfer processes [25], between 1 kHz and 100 Hz, see Supplementary Information SI 1. For a more detailed discussion on this method, it is referred to Ref. [16]. For the analysis of the HFR of the cell segments, the measurement quality is too low to be properly evaluated at current densities <1 A•cm^{-2}, see discussion in Ref. [4]. For current densities <1 A•cm^{-2} the HFR between 1 A•cm^{-2} and 2 A•cm^{-2} is linearly interpolated and the extrapolated towards lower current densities. At every operation point, the current density and temperature of the cell segments are measured. To analyze the local cell behavior, the cell is operated at constant current (galvanostatic) mode. Constant voltage (potentiostatic) mode is beneficial at critical operation points to analyze limiting currents, which is therefore

conducted as well. Furthermore, at specific current densities (galvanostatic) EIS is conducted between 10 kHz and 100 mHz to analyze, in addition to the HFR, the polarization resistance of the mean cell and the cell segments.

2.5. Impedance analysis

Before each impedance analysis, the generated data is tested for drift and instabilities using the Kramers Kronig test [26,27]. The impedance spectra shown in this work fulfill the Kramers Kronig test with the residuals being smaller than ±1%. For critical impedance data (Kramers Kronig residuals greater than ±1%) that can occur during undersupply of reactant (water) in the cell it is explicitly mentioned that the data should be interpreted with caution.

Polarization processes often occur at similar time constants leading to an overlapping of each other. In conventional Nyquist plots or Bode presentations these processes can often not be deconvoluted accurately. Distribution of Relaxation Time (DRT) has proven to be a useful method for several electrochemical converters, such as batteries, fuel cells and electrolysis cells [28–33]. In this work a DRT algorithm developed by KIT is used [34]. With DRT, the number of relevant processes can be estimated by the number of peaks in the DRT function $g(\tau)$, which can be calculated by Equation (1).

$$Z(\omega) = R_0 + R_{\text{pol}} \int_0^\infty \frac{g(\tau)}{1 + j\omega\tau} d\tau \qquad (1)$$

R_0 describes the ohmic resistance of the cell which should correspond to the values determined by HFR measurements, see above. R_{pol} is the sum of the resistance of all polarization processes. Solving Equation (1) is challenging, a widely employed approach is the use of the regularization parameter λ by Tikhonov [35,36]. In our previous impedance analysis for this test setup the optimal Tikhonov parameter was determined to be $\lambda = 10^{-3}$, see Ref. [4], which is also used in this study. It is here to be mentioned that minimal inaccuracies in the measurement can provoke DRT peaks, which can lead to misinterpretations [37], which is circumvented using the Kramers Kronig test, see above.

In our previous work we showed the importance of the low-frequency inductive feature [38,39]. Within this work, we discuss the superimposing phenomena of inductive loops and mass transport related polarization due to reactant undersupply. The DRT algorithm by KIT was previously adapted to analyze low-frequency inductive loops and interpret them as RC-elements allowing negative resistance values [40].

3. Results & discussion

3.1. Polarization curve measurements under water starvation

At low flow rates, the stoichiometry serves as an important reference value. The stoichiometry λ directly correlates the consumed water ($\dot{n}_{\text{w,stoich}}$) with the amount of water applied ($\dot{n}_{\text{w,app}}$), defined by Equation (2).

$$\lambda = \frac{\dot{n}_{\text{w,app}}}{\dot{n}_{\text{w,stoich}}} = \frac{z \cdot F \cdot \dot{V}_{\text{w,app}} \cdot \rho_{\text{w}}}{i \cdot A \cdot M_{\text{w}}} \qquad (2)$$

With M_{w} and ρ_{w} being the molar mass and density (at the operational temperature) of water, $\dot{V}_{\text{w,app}}$ the applied volume flow of water, z the number of transferred electrons, F Faraday's constant, i the mean cell current density, and A the active cell area. As discussed in the Introduction section, PEM water electrolyzers are typically operated under water enrichment ($\lambda > 100$) at which no severe humidification issues of membrane and ionomer are present [3,15]. At $\lambda < 10$ water deficits are reported in the literature, resulting in increasing Ohmic resistance due to not properly humidified membrane and ionomer [6,12,41].

Fig. 2 shows the performance analysis of the entire AtC cell under water starvation in galvanostatic operation. The polarization curves and HFR-free polarization curves (dashed lines at the bottom) reveal that operations with 107 µl•min^{-1}•cm^{-2} (red curve) and 161 µl•min^{-1}•cm^{-2} (yellow curve) anode water flow, are consistent with each other but differ from the measurement with high water flow rate of 10.7 ml•min^{-1}•cm^{-2} (black curve) significantly, as shown in Fig. 2 a). At current densities <4 A•cm^{-2} and a high water flow rate a significantly better performance is measured which can be attributed to a temperature effect. With high water flow rates, the cell is properly heated by the inlet water which results in a low and slightly decreasing HFR with increasing current density, see Fig. 2 b). The mean cell temperature measured by the 120 temperature sensors within the PCB underneath the anode flow field increases by 9 K from low to high current densities, see Fig. 2 c). The error bars represent the standard deviation of all 120 temperature sensors alongside the active area.

However, at 107 µl•min^{-1}•cm^{-2} and 161 µl•min^{-1}•cm^{-2}, the mean cell temperature measured with the PCB changes significantly with current density. At low current densities, the cell temperature is around 39 °C, which is explained by the heat loss between CCM and PCB (23 mm
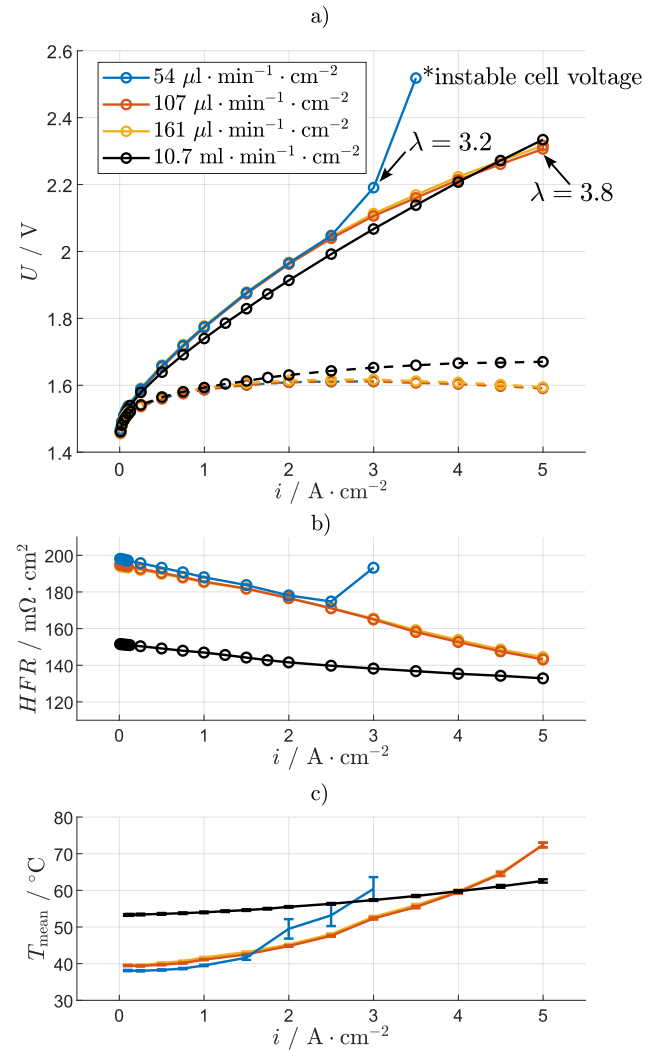

Fig. 2. Cell behavior of the entire AtC cell under variation of the flow rate. a) Polarization curve and HFR-free polarization curve, b) HFR over current density, and c) mean cell temperature measured with the PCB at a flow rate variation between 54 µl•min^{-1}•cm^{-2} and 161 µl•min^{-1}•cm^{-2} and compared with industrially relevant high flow rates. The measurements are done at 60 °C (inlet water temperature) and ambient pressure.

distance in height) and the small amount of water (at 60 °C) supplied to the cell. With increasing current density, the mean cell temperature rises up to 72 °C, indicating the poor heat management due to the low water flow rate. The intersection of the temperature curves of 107 µl•min^{-1}•cm^{-2} and 161 µl•min^{-1}•cm^{-2} with 10.7 ml•min^{-1}•cm^{-2} at ~4 A•cm^{-2} agrees with the intersection of the polarization curves. This temperature effect also explains the lower cell overpotentials, see HFR-free polarization curve. Since the differences for 107 µl•min^{-1}•cm^{-2} and 161 µl•min^{-1}•cm^{-2} in cell performance and temperature are small (10 mV), we believe that no significant undersupply of water and therefore no pertinent membrane dry-out is present. Even at 5 A•cm^{-2} and 107 µl•min^{-1}•cm^{-2} with a stoichiometry of $\lambda < 4$, the cell operation seems to be stable. However, the low water flow rates suggest that the membrane conductivity is reduced due to non-optimal membrane humidification, which can be assumed for the high water flow of 10.7 ml•min^{-1}•cm^{-2} applied. It should be noted that the here detected temperature influence is enormous and needs to be considered when analyzing the data. An improved external heat management, e.g. by using a thermal surrounding at operation temperature (thermal box) may significantly reduce this inaccuracy.

For the measurement with a water flow rate of 54 µl•min^{-1}•cm^{-2}, comparable cell behavior is measured up to 2 A•cm^{-2} with only slightly higher HFR and lower temperature compared with 107 µl•min^{-1}•cm^{-2} and 161 µl•min^{-1}•cm^{-2}. Above a current density of 2 A•cm^{-2} ($\lambda \sim 4.8$) the cell performance is decreasing drastically, as both the HFR and cell temperature increase. The error bars of the mean cell temperature indicate unstable cell behavior during operation, since large temperature differences along the channel occur. When the current density is set from 3 A•cm^{-2} to 3.5 A•cm^{-2}, a linear increase of the cell voltage from 2.3 V to 2.7 V was observed for the first 70 s, reaching exponentially within the next 20 s the voltage limit of 3.5 V of the test bench, see Supplementary Information SI 2. Due to the increasing HFR paired with increasing cell temperature but not affected cell polarization (see HFR-free polarization curve) up to 3 A•cm^{-2} the measurement suggests that the cell faced significant membrane dry-out, which is analyzed in the following using impedance spectroscopy.

At 3 A•cm^{-2}, a stoichiometry of 3.2 can be calculated with significant dry-out effects detected. Since even at higher stoichiometries ($\lambda \sim 4.8$ at 2 A•cm^{-2}) these effects start to occur and at a flow rate of 107 µl•min^{-1}•cm^{-2}, stoichiometries of $\lambda \sim 3.8$ do not seem to be affected by dry-out, we conclude that only considering the stoichiometry cannot provide sufficient information on relevant membrane and ionomer dry-out. Instead, more parameters as local temperature, ratio of liquid and vapor phase of water, membrane-specific electro-osmotic drag and properties of the porous materials need to be considered.

3.2. Impedance analysis of the entire cell under water starvation

Impedance spectroscopy of the entire cell, applied at current densities of 1 A•cm^{-2} and 3 A•cm^{-2} during the polarization curve reveals significant differences in performance, see Nyquist presentations of Fig. 3 a) and b). At a current density of 1 A•cm^{-2} the polarization resistance appears to be comparable for all flow rates applied, and only differences in the HFR are detected. This is consistent with the results in Fig. 2, as all HFR-free polarization curves show equal behavior for 1 A•cm^{-2}.

At 3 A•cm^{-2}, in addition to the change in HFR, which is discussed above, also the polarization resistances change. The capacitive loop at higher frequencies, which we refer to charge transfer processes, does not significantly differ among the measurements. The difference between the HFR and the low frequency resistance (LFR, real part of the impedance at the second intersection with -Im(Z) = 0) is for all spectra around 15 mΩ•cm^2. This can also be seen at the DRT analysis in Fig. 3 c) between 25 Hz and 1 kHz. The processes appear to occur at similar frequencies and show comparable area-specific-resistance (ASR), see area underneath each peak. This indicates that, although significant
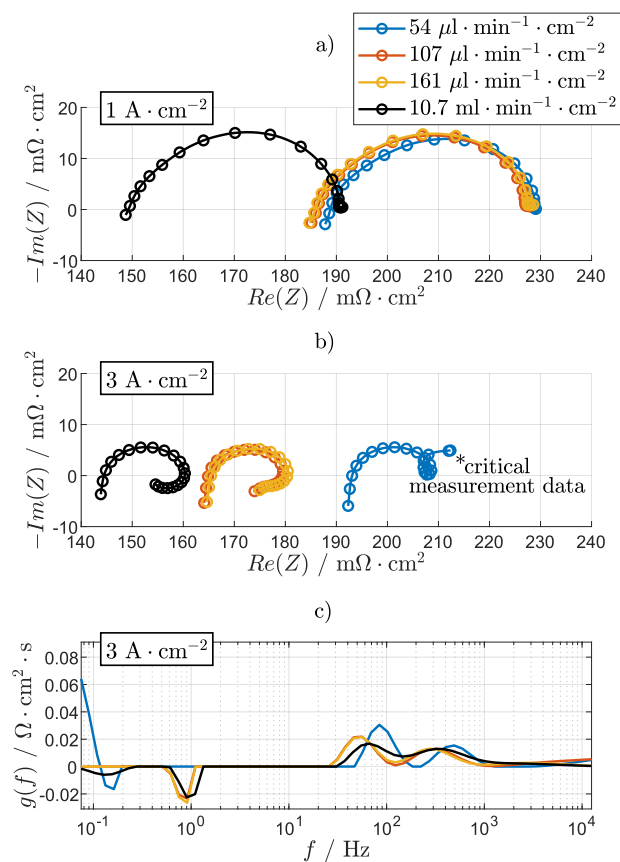

Fig. 3. Impedance analysis of the mean cell at stoichiometry variation. Nyquist presentation at a) 1 A•cm^{-2} and b) 3 A•cm^{-2}, and c) DRT analysis at 3 A•cm^{-2}. The measurements are done at 60 °C (inlet water temperature) and ambient pressure.

differences in water supply are present, the charge transfer resistance is not significantly affected.

Contrary to this, the low-frequency impedance below 2 Hz differs among the measurements, as a typical inductive loop is detected at high flow rates, which is in good agreement with our previous findings [38, 39]. The physico-chemical processes behind the inductive features are not yet fully understood. In our previous works, we suggested that slow processes which decrease the membrane resistance due to water diffusion or thermal effects might be the origin of this phenomenon. In the DRT analysis, two inductive peaks are detected at ~1 Hz and ~130 mHz for 10.7 ml•min^{-1}•cm^{-2} water flow applied. For the 107 µl•min^{-1}•cm^{-2} and 161 µl•min^{-1}•cm^{-2} the inductive feature at ~1 Hz is also detectable and comparable with 10.7 ml•min^{-1}•cm^{-2}. The second inductive process can only be anticipated by the change of the arc in the Nyquist presentation. This process is not detected by the DRT algorithm within the measurement range.

For a water flow rate of 54 µl•min^{-1}•cm^{-2}, the inductive loop is overlapped by a second capacitive loop which is usually related to mass transport losses or limitations of the reactant, as described in PEM fuel cells and water electrolyzers literature [42–46]. The small inductive process at around 150 mHz is superimposed by a comparably large capacitive process according to the DRT analysis, indicating that severe mass transport resistance is present. In general, this impedance measurement at low flow rates needs to be considered carefully as the cell performance behaves unstable, reaching the limits of the Kramers Kronig residuals of ± 1%. This is especially pressing for the low-frequency range, see dashed lines in the Nyquist presentation. However, with impedance analysis, we can show that mass transport limitations (second capacitive loop at low frequencies) for water as a reactant occurs

simultaneously with increasing membrane resistance (increase of HFR) resulting in a large increase of the mean cell resistance.

3.3. Local impedance analysis under water starvation

Up to this point, we only discussed the performance behavior of the entire AtC cell. The locally resolved impedance spectra at a mean current density of 3 A•cm^{-2} and water flow rates of 54 μl•min^{-1}•cm^{-2}, 107 μl•min^{-1}•cm^{-2} and 161 μl•min^{-1}•cm^{-2} are depicted in Fig. 4. Fig. 4 a) shows the HFR-free Nyquist presentation at 54 μl•min^{-1}•cm^{-2} for all 10 segments, the corresponding spectra at 107 μl•min^{-1}•cm^{-2} and 161 μl•min^{-1}•cm^{-2} are provided in the Supplementary Information SI 3. The HFR distribution along the channel is presented in Fig. 4 b) at the top. The HFR measured at 161 μl•min^{-1}•cm^{-2} water flow shows a homogenous profile with a maximum spread of ~ 17 mΩ·cm^2 which is referred to contact issues of the segments and the temperature gradient of ~5 K along the channel, see Fig. 4 b) at the bottom. It should be noted that the temperature shown here is measured using the PCB and not the water temperature. Due to heat loss between CCM and the measurement

contacts of the PCB temperatures underneath the inlet water temperature are observed. The current density profile (center) also shows a homogenous distribution. At 107 μl•min^{-1}•cm^{-2} equal cell behavior as at 161 μl•min^{-1}•cm^{-2} [1] is observed, with a slightly higher HFR for segment 9 and segment 10.

At 54 μl•min^{-1}•cm^{-2} higher current densities at the inlet and lower at the outlet are detected with increased HFR-values from segment 3 onwards. The temperature profile stays rather constant between segments 1 and 5 and is drastically increasing by 20 K between segments 6 and 10. These effects can clearly be attributed to undersupply, local dryout of ionomer and membrane and heating up of the segments.

The polarization resistance along the channel supports these findings, see Fig. 4 a) and the DRT analysis in Fig. 4 c). For 54 μl•min^{-1}•cm^{-2} segment 1 exhibits an impedance spectrum with a proper water supply, as two capacitive peaks at ~400 Hz and ~70 Hz, and two inductive features at ~1 Hz and below 200 mHz are detectable. Segment 2 already shows a slight superimposition of the inductive loop by a low-frequency capacitive loss process; see Fig. 4 a). For segment 3 to 7 the low-frequency capacitive process is increasing and the negative
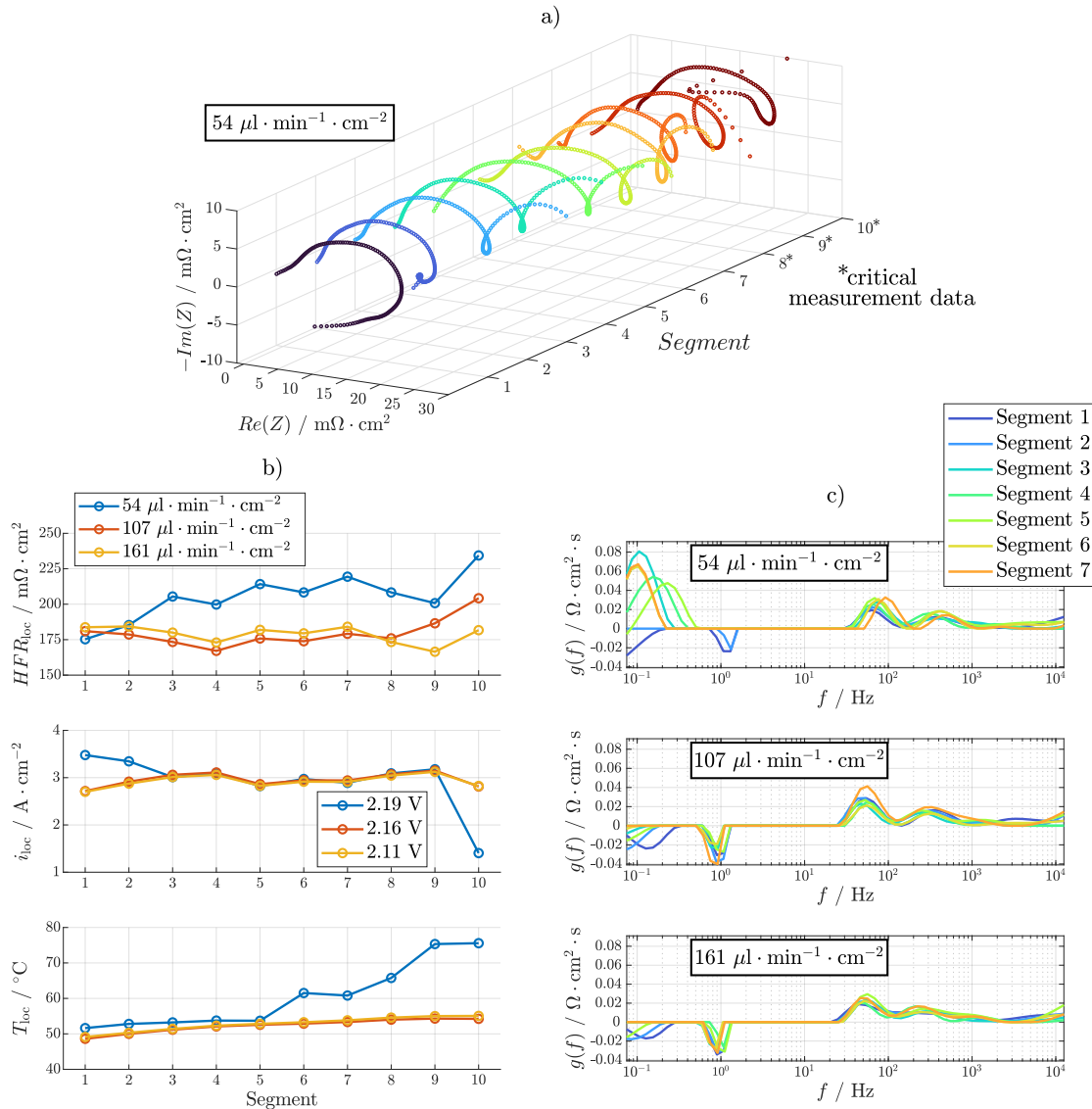
Fig. 4. Locally resolved performance analysis under flow rate variation. a) HFR-free Nyquist presentation at a water flow rate of 54 μl•min^{-1}•cm^{-2}, b) current density, HFR, and temperature distribution, and c) DRT analysis of segment 1 to 7 at 54 μl•min^{-1}•cm^{-2}, 107 μl•min^{-1}•cm^{-2} and 161 μl•min^{-1}•cm^{-2} anode water flow. The measurements are done at 60 °C (inlet water temperature) and ambient pressure.

peak vanishes, indicating that the inductive loop is superimposed by an increasing mass transport resistance. Segment 8 to 10 show highly unstable condition and do not fulfill the Kramers Kronig test at low frequencies, reaching residuals of up to ±27%. Therefore, these spectra are not further analyzed with DRT and not discussed here. The instability portends the critical situation due to water starvation. The measurements at 107 μl•min^{-1}•cm^{-2} and 161 μl•min^{-1}•cm^{-2} water flow rate show DRT behavior comparable to 100 ml•min^{-1}•cm^{-2}, neither temperature or HFR increase, nor significant mass transport related processes were observable over the entire active area.

3.4. Current density distribution analysis under water starvation

Since the cell shows highly unstable behavior in galvanostatic mode when operating close to the stoichiometric level, we analyze the current density distribution under flow rate variation in potentiostatic mode, at a cell voltage of 2.4 V, see Fig. 5 a). For easier comparison of the results, the deviation of the local current density from the mean current density is shown over the cell segments. Each mean current density is given in the legend. At a flow rate of 161 μl•min^{-1}•cm^{-2} only marginal deviations of up to 8 % are detected. These deviations are related to contact issues of the segments (e.g. see segment 4 and 7) and to a temperature effect. Accumulating gas leads to poorer heat removal along the channel, which results in increased heating of the components, such as the membrane. In turn, increased temperature of the membrane leads to increased membrane conductivity, therefore, (slightly) more current is flowing at the outlet compared to the inlet, see temperature profile in Fig. 5 b).

At 107 μl•min^{-1}•cm^{-2} water flow, a comparable trend is observed between segment 1 and segment 8. However, at segment 9 and 10 a drop
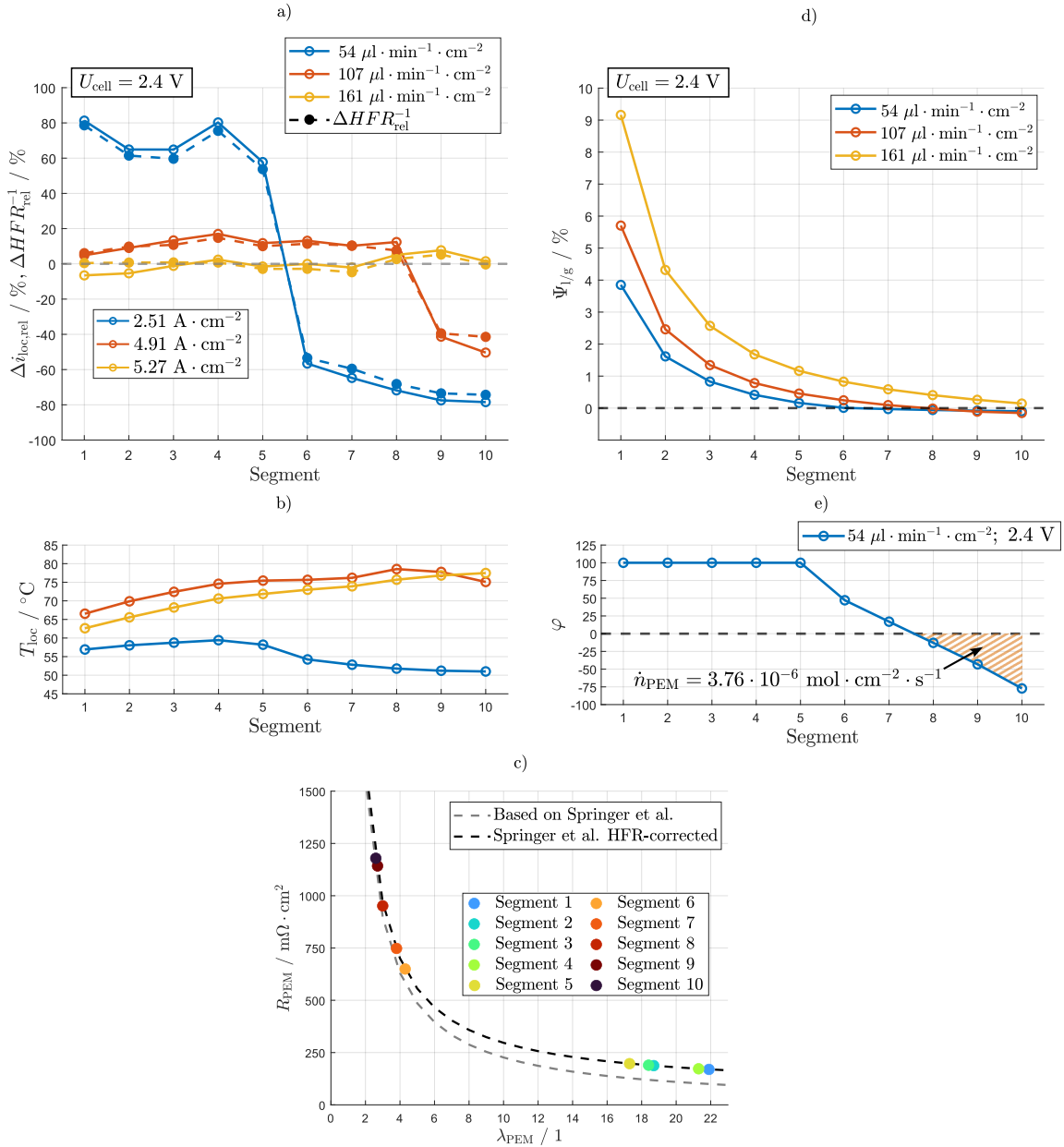
Fig. 5. a) Relative deviation of the mean current density ($i_{loc,rel}$) at 2.4 V and water flow rate variation. The relative deviation of the inverse HFR (HFR_{rel}^{-1}) is given in dashed lines, b) corresponding temperature profiles. c) Membrane resistance over water content of the membrane according to Refs. [48,49], d) calculation of the liquid-to-gas ratio, and e) calculation of the relative humidity over the cell segments. The measurements are done at 60 °C (inlet water temperature) and ambient pressure.

in current density compared to the mean current density of -40% and -50%, respectively, is detected. The current density drop may be explained by a beginning of water starvation since a high amount of reactant was consumed by the previous segments. Even lower flow rates of 54 μl•min^{-1}•cm^{-2} shows that this current density drop seemingly moves more towards the cell inlet, as the drop occurs already at segment 6 with up to -78% deviation from the mean value. These almost inactive segments lead to a current density increase at the first 5 segments. However, the mean current density is drastically reduced compared with the other measurements, see legend at the bottom left. It should be noted, that the potentiostatic measurements were conducted after the galvanostic measurements as presented in Fig. 2. Since these harsh measurements clearly harmed the cell components, a significant decrease in overall performance is observed. Several degradation effects need to be considered, as oxidation of PTL and flow field components as well as deactivation of the catalyst layer. However, due to the operation enforcing dry-out, we would assign most of the degradation effects to change of ionomer and membrane properties. Investigations of these degradation effects are not focus of this study but is highly recommended to gain more understanding. Characterization methods, such as EIS, cyclic voltammetry, and ex situ analyses as discussed for PEM fuel cell stacks in Ref. [47] are expected to be highly valuable.

The Supplementary Information SI 4 shows the analysis at 2.0 V and 2.2 V r revealing that no local dry-out occurs at 2.0 V for all water flow rates. For 54 μl•min^{-1}•cm^{-2} and 2.2 V the above discussed current density drop was observed for segment 8 to 10. It also can be seen that the mean cell current density between 2.2 V and 2.4 V is only marginally increasing, which suggests that operation close to a limiting current is present. The temperature profiles show an increasing trend along the segments whenever a relatively constant current profile is present, as the current density drops down (at segment 9 for 107 μl•min^{-1}•cm^{-2} and segment 6 for 54 μl•min^{-1}•cm^{-2} at 2.4 V) the cell cools down due to less heat dissipation from the reaction, see Fig. 5 b). This can be interpreted as a critical situation regarding water supply, but no total membrane drying occurs, as compared with increasing temperature and increasing HFR for 2.4 V in Fig. 5.

During these potentiostatic measurements locally resolved impedance measurements were carried out to extract the HFR of each individual segment using the approach mentioned above. Especially at 54 μl•min^{-1}•cm^{-2} the impedance data quality and thus the accuracy is low which needs to be carefully considered. The fitting error for the HFR analysis is determined to be $<12\%$. The HFR measurements discussed here should only be seen in a qualitative way.

According to Ohm's law, the current (density) is at constant voltage inversely proportional to the resistance, see Equation (3).

$$\Delta i_{\text{loc,rel}} \propto \Delta R_{\text{loc,rel}}^{-1} \; \text{with } U_{\text{loc,rel}} = U_{\text{cell}} \tag{3}$$

plotted in Fig. 5 a) with dashed lines, showing high agreement for all measurements. The marginal deviations between current density and inverse HFR are attributed to the poor impedance quality.

$$\Delta i_{\text{loc,rel}} \propto \Delta \text{HFR}_{\text{loc,rel}}^{-1} \; \text{with } U_{\text{loc,rel}} = U_{\text{cell}} \tag{4}$$

To understand the characteristic drop in current density for 54 μl•min^{-1}•cm^{-2} and 107 μl•min^{-1}•cm^{-2} at segment 6 and segment 9, respectively, an estimation of the water content of the membrane λ_{PEM} is performed, see Fig. 5 c). Springer, Zawodzinski et al. discussed the influence of λ_{PEM} on various membrane parameter of Nafion-based membranes, such as membrane conductivity [48,49]. They observed a saturation of the water content, which is seen as fully humidified at $\lambda_{\text{PEM}} = 22$. It is assumed that the first segment during the measurement at 2.4 V and 54 μl•min^{-1}•cm^{-2} equals a water content of $\lambda_{\text{PEM}} = 22$. Therefore, the measurement data reported by Springer is corrected by the HFR of the first segment, see black dashed line. Segment 1 to segment 5 range in between $17 < \lambda_{\text{PEM}} < 22$, which is seen as the region between fully vapor-saturated and saturated with liquid water. In contrast, the water content of segment 6 to segment 10 ranges between $2.6 < \lambda_{\text{PEM}} < 4.3$, which indicates the severe membrane drying. Between segment 5 and segment 6 a change in HFR of > 450 mΩ•cm^2 is observed, which leads to the interpretation that in segment 5 all liquid water is consumed and segment 6 to segment 10 is only supplied by water in the vapor phase.

To evaluate this interpretation, a calculation of the liquid-to-gas ratio $\Psi_{\text{l/g}}$ along the cell segments in the anode flow field channel for a flow rate variation of 54 μl•min^{-1}•cm^{-2} at 2.4 V cell voltage is presented in Fig. 5 d). Utilizing the information about the current flowing through each segment and the inlet water, the liquid-to-gas ratio in the flow field channels is calculated for each segment, see Equation (5). It is assumed that the amounts of liquid water, gaseous water and oxygen at the end of one segment equals the inlet of the next segment. It is presumed that the oxygen produced has a relative humidity of 100 % if liquid water is present. The amount of vapor water is calculated using the saturated vapor pressure using Antoine's equation [50], which is then subtracted from the liquid water amount and added to the gas phase. The electro-osmotic drag is assumed to be constant over the whole active area, independent of membrane humidification, pressure, and temperature. Literature suggests a drag coefficient between $0.9 < \zeta < 7$ (molecules of water per proton) depending on the membrane humidification [49,51,52]. If the current density drop between segment 5 and segment 6 is caused by the transition between liquid and vapor-fed electrolysis, a drag coefficient of $\zeta = 3$ can be fitted, which is in good agreement with literature values. The water diffusion and back diffusion through the membrane and the presence of vapor water are not considered here.

$$\Psi_{\text{l/g,j}} = \Psi_{\text{l/g,j}-1} - \frac{\dot{V}_{\text{l,j}-1} - \dot{V}_{\text{l,j}}}{\sum_1^{j-1} \dot{V}_{\text{g,prod}} + \dot{V}_{\text{g,j}}} = \Psi_{\text{l/g,j}-1} - \frac{\overbrace{\dot{V}_{\text{l,j}-1}}^{\text{previous segment}} - \overbrace{\left(\frac{i_j \cdot M_w \cdot (1+\zeta)}{z \cdot F \cdot \rho_w}\right)}^{\text{water consumption by reaction}} - \overbrace{\left(\frac{i_j \cdot M_w}{z \cdot F \cdot \rho_w} \frac{p_s(T)}{p_{\text{cell}} - p_s(T)}\right)}^{\text{water evaporation}}}{\underbrace{\sum_1^{j-1} \dot{V}_{\text{g,prod}}}_{\text{previous segment}} + \underbrace{i_j \cdot R \cdot T_j / z \cdot F \cdot p_{\text{cell}}}_{\text{gas production by reaction}} + \underbrace{\left(\frac{i_j \cdot R \cdot T_j}{z \cdot F \cdot p_{\text{cell}}} \frac{p_s(T)}{p_{\text{cell}} - p_s(T)}\right)}_{\text{water evaporation}}} \quad \text{with } 1 \leq j \leq 10 \tag{5}$$

With the assumption that a change in HFR is mostly depending on the change of membrane resistance due to humidification (at comparable temperatures) we can state that a direct correlation between the inverse HFR and current density distribution explains local membrane dry-out, see Equation (4). Therefore, the relative deviation of the inverse HFR is

i_j describes the current in segment j, M_w the molar mass and ρ_w the density of water, z the number of electrons transferred, F Faraday's constant, and R the universal gas constant. The temperature of each segment T_j is measured by the PCB, the temperature in the catalyst layer might be significantly higher, as heat dissipation between CCM and PCB

is expected, as discussed previously [4]. Since the pressure drop along the channel is < 300 mbar, the pressure in the segments is assumed to be constant and equal to the cell pressure p_{cell}, $p_s(T)$ describes the saturated water pressure. The inlet liquid-to-gas ratio is set as a boundary condition to $\Psi_{l/g,0} = 100$ %.

For 161 µl•min^{-1}•cm^{-2} a minimum liquid-to-water ratio of 0.13 % at segment 10 is observed, which seems to adequately feed the electrolysis reaction and humidifies the membrane since no decrease of current density towards the cell outlet is observed, see Fig. 5 a). For 107 µl•min^{-1}•cm^{-2} from segment 8 and for 54 µl•min^{-1}•cm^{-2} from segment 6, negative liquid-to-gas ratios are observed. Both values are in good agreement with the characteristic current density drop, which is interpreted as transition between liquid and vapor-fed electrolysis. The slight inaccuracy for 107 µl•min^{-1}•cm^{-2} (negative values from segment 8 but current density drop at segment 9) is attributed to the neglected water diffusion and homogenous drag coefficient.

At a negative liquid-to-gas ratio, the reaction is fed by vapor water, which can be calculated by the relative humidity φ as the vapor-water uptake of the produced oxygen. Fig. 5 e) shows the relative humidity for 2.4 V and 54 µl•min^{-1}•cm^{-2}. If liquid water is present (from segment 1 to segment 5) a relative humidity of 100 % is assumed. As the vapor-fed electrolysis is present from segment 6 on, the water amount in vapor phase accumulated between segment 1 and segment 5 supplies the reaction. Therefore, the relative humidity decreases along the channel. At segment 8 to segment 10 negative values for the relative humidity are observed, which are non-physical. One interpretation may be that these cell regions are fed by back diffusion water through the membrane from accumulated drag water at the cathode, which is not considered in our calculations. The stoichiometric water flux which cannot be covered by our calculation (segment 8 to segment 10, see orange dashed area) is $\dot{n}_{stoich,8-10} = 3.76\cdot10^{-6}$ mol·cm^{-2}·s^{-1}, which needs to be provided by the back diffusion flux $\dot{n}_{PEM}$, see Fig. 5 e). This value for the here used Nafion® N115 membrane is in the same order of magnitude as the values determined in the experimental permeation studies in the literature [53,54].

3.5. Influence of gas pressure under water starvation

Water transport to the catalyst layer competes with the opposing removal of oxygen through PTL and flow field. Since water can be assumed to be incompressible, but gas transport is significantly affected by pressure, the cell pressure at both sides (balanced pressure) was set to 0 bar$_g$, 3 bar$_g$, and 6 bar$_g$ in potentiostatic operation, see Fig. 6. Fig. 6 a) depicts the current density profiles with a water flow rate of 54 µl•min^{-1}•cm^{-2} at 2.0 V, 2.2 V, and 2.4 V, respectively, and the different pressures applied. At 2.0 V, inactive segments are not observable at all, as all graphs show equal current density distribution, for even lower voltages as well no inactive segments are expected, as also identifiable for 54 µl•min^{-1}•cm^{-2} flow rate in Fig. 2 and Supplementary Information SI 4. The mean cell current densities for each cell voltage are provided in the legend and in Fig. 6 b). A slightly lower performance with increased pressure is observed at a given cell voltage of 2.0 V which is attributed to increased Nernst potential [55] and setup-depending increased HFR, as shown in Fig. 6 c). The HFR slightly increases with pressure since the contact between PTL and flow field decreases, as previously discussed for differential pressure operation with a comparable setup [4]. We believe that a similar phenomenon occurs as well with balanced pressure operation and might be even more pronounced due to the anode pressure, leading to further detachment of the PTL from the flow field lands.

At 2.2 V and at 0 bar$_g$ and 3 bar$_g$ pressure, a drop in current density is observed at segments 8 to 10, which is not detected under 6 bar$_g$ pressure. Additionally, the mean cell current densities and HFR values change, with the highest pressure showing the best cell performance. The change in HFR at these low water flow rates is associated with local
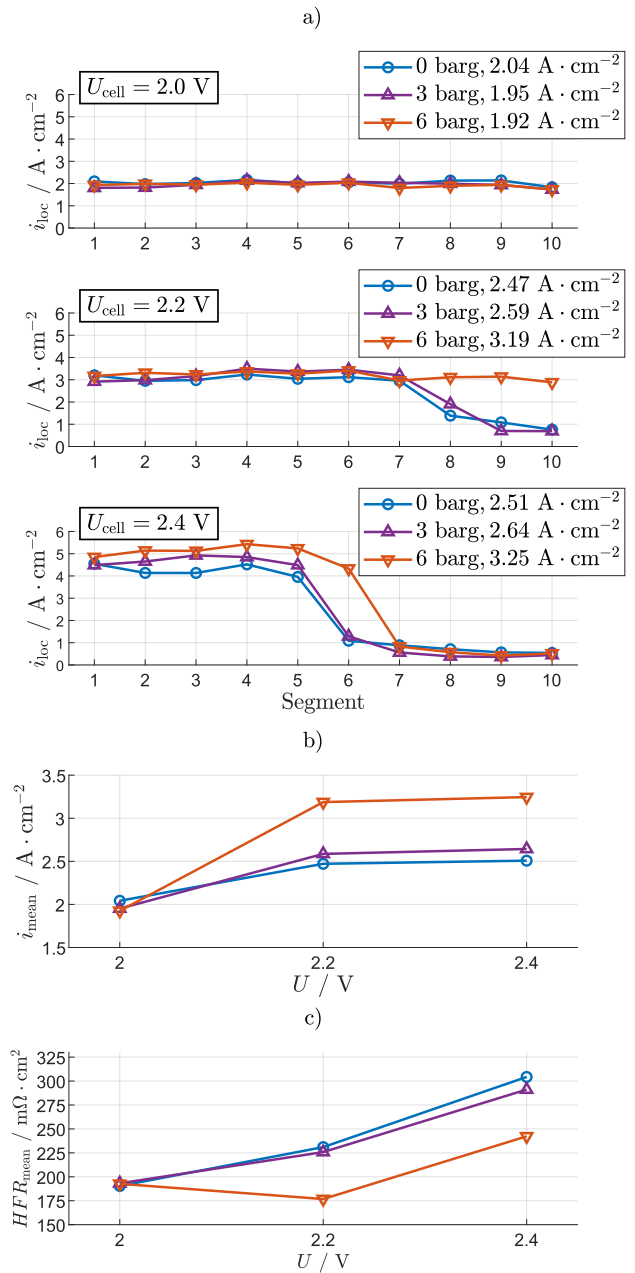
Fig. 6. a) Current density distribution at 2.0 V, 2.2 V and 2.4 V cell voltage for 0 barg, 3 barg and 6 barg balanced cell pressure, b) mean current density and c) mean HFR over cell voltage. The measurements are done at 60 °C (inlet water temperature) and a water flow rate of 54 µl•min^{-1}•cm^{-2}.

membrane dry-out. At 2.4 V, all pressure conditions result in a drop in local current density towards the cell outlet. However, the current density profiles, mean cell current densities and the HFR suggest that pressure operation leads to less critical dry-out effects.

4. Conclusion

This work discusses the behavior of a PEM water electrolysis cell at high current densities up to 5 A•cm^{-2} under water starvation with water stoichiometries of <10. Water flow rates between 54 µl•min^{-1}•cm^{-2} and 161 µl•min^{-1}•cm^{-2} were applied to an along the channel test cell with an active area of 56 cm^2 and compared with a standard flow rate of 10.7 ml•min^{-1}•cm^{-2}. Water stoichiometries above 5 do not show significant mass transport-related limitations, even at high current

densities of 5 A•cm^{-2}, which is in good agreement with the literature [6, 12]. When operating at stoichiometries of approximately 3, significant increase of the HFR, which we associate with membrane dry-out, is observed, resulting in unstable cell voltages. An increase in mass transport resistance has been detected when operating close to the stoichiometric water level, superimposing low-frequency inductive features analyzed by electrochemical impedance spectroscopy.

Locally resolved impedance analysis showed that even when operating close to the stoichiometric level, inlet segments were still properly supplied with water, while segments towards the cell outlet showed local membrane drying and increased mass transport resistance. Segments at the cell outlet exhibited unstable behavior, which drastically affected the quality of impedance data.

Under potentiostatic operation, we demonstrate that there is a direct correlation between the current density distribution and the distribution of the inverse high frequency resistance, which we refer to as membrane conductivity. Comparison to experimental studies of membrane conductivity depending on the membrane's water content shows that severe membrane dry-out is present at the cell outlet. Theoretical calculations of the liquid-to-gas ratio show that at characteristic current density drops, no liquid water is present anymore and that the reaction might be covered by the humidity of the oxygen produced. The relative humidity of the gas is therefore decreasing along the channel, resulting in negative values, which are interpreted as back diffusion of water through the membrane, and are neglected in the calculation. A quantitative comparison of the missing stoichiometric water flux has the same order of magnitude as experimental analyses of the same membrane reported in the literature.

Varying the cell pressure revealed that increased gas pressure can reduce dry-out effects. This is attributed to the reduced volume demand of the gas transport from the catalyst layer through the PTL and subsequently the improved water transport to humidify the ionomer and membrane.

In summary, it can be stated that, for the herein used cell setup, the limiting factor of operation under water starvation is an increasing membrane resistance, due to dry-out. Increase of low-frequency capacitance in impedance data, which is attributed to mass transport processes, are observed simultaneously, indicating water transport limitations. The operation presented in this work may not be typical for PEM water electrolysis, which is usually conducted at water stoichiometries >100, but it highlights the importance of proper water distribution. This is especially pressing for large industry stack designs. Given the severe impact on cell performance observed under these extreme conditions, further investigations into degradation under full or partial water supply are recommended. Moreover, electrochemical and fluidic modeling is suggested to better understand the limiting factors of water supply to the anode.

CRediT authorship contribution statement

Niklas Hensle: Writing – original draft, Visualization, Validation, Project administration, Methodology, Investigation, Formal analysis, Data curation, Conceptualization. **Thomas Lickert:** Writing – review & editing, Validation. **Nico Winterholler:** Writing – original draft, Investigation. **Tom Smolinka:** Writing – review & editing, Supervision, Project administration, Funding acquisition, Conceptualization. **André Weber:** Writing – review & editing, Supervision, Project administration, Funding acquisition, Formal analysis, Conceptualization.

Declaration of competing interest

The authors declare that they have no known competing financial interests or personal relationships that could have appeared to influence the work reported in this paper.

Acknowledgment

Appendix A. Supplementary data

Supplementary data to this article can be found online at https://doi.org/10.1016/j.jpowsour.2025.237865.

Data availability

Data will be made available on request.

References

[1] N. Hensle, T. Smolinka, Understanding mass transport at high current densities in an industrial scale PEM electrolysis test cell - a segmented along-the-channel approach, Meet. Abstr. (34) (2024) 1849. MA2024-01.

[2] T. Lickert, S. Fischer, J.L. Young, S. Klose, I. Franzetti, D. Hahn, et al., Advances in benchmarking and round robin testing for PEM water electrolysis: reference protocol and hardware, Appl. Energy 352 (2023) 121898.

[3] O. Panchenko, L. Giesenberg, E. Borgardt, W. Zwaygardt, N. Kardjilov, H. Markötter, et al., Influence of stoichiometry on the two-phase flow behavior of proton exchange membrane electrolyzers, Energies 12 (3) (2019) 350.

[4] N. Hensle, J. Horstmann de la Viña, N. Winterholler, J. Hoffmann, S. Armbruster, A. Lindner, et al., Understanding the cell performance along the channel for industrial PEM water electrolysis operation, ACS Appl. Energy Mater. 8 (11) (2025) 7107–7124.

[5] K.E. Ayers, E.B. Anderson, C. Capuano, B. Carter, L. Dalton, G. Hanlon, et al., Research advances towards low cost, high efficiency PEM electrolysis, ECS Trans. 33 (1) (2010) 3–15.

[6] C. Immerz, B. Bensmann, P. Trinke, M. Suermann, R. Hanke-Rauschenbach, Local current density and electrochemical impedance measurements within 50 Cm single-channel PEM electrolysis cell, J. Electrochem. Soc. 165 (16) (2018) F1292–F1299.

[7] A. Mayyas, M. Ruth, B. Pivovar, G. Bender, K. Wipke, Manufacturing Cost Analysis for Proton Exchange Membrane Water Electrolyzers, 2019.

[8] M. Müller, M. Carmo, A. Glüsen, M. Hehemann, S. Saba, W. Zwaygardt, et al., Water management in membrane electrolysis and options for advanced plants, Int. J. Hydrogen Energy 44 (21) (2019) 10147–10155.

[9] X. Guan, J. Bai, J. Zhang, N. Yang, Multiphase flow in PEM water electrolyzers: a mini-review, Curr. Opin. Chem. Eng. 43 (2024) 100988.

[10] C. Immerz, M. Schweins, P. Trinke, B. Bensmann, M. Paidar, T. Bystroň, et al., Experimental characterization of inhomogeneity in current density and temperature distribution along a single-channel PEM water electrolysis cell, 0013-4686 260 (2018) 582–588.

[11] J. Parra-Restrepo, R. Bligny, J. Dillet, S. Didierjean, D. Stemmelen, C. Moyne, et al., Influence of the porous transport layer properties on the mass and charge transfer in a segmented PEM electrolyzer, Int. J. Hydrogen Energy 45 (15) (2020) 8094–8106.

[12] S. Sun, Y. Xiao, D. Liang, Z. Shao, H. Yu, M. Hou, et al., Behaviors of a proton exchange membrane electrolyzer under water starvation, RSC Adv. 5 (19) (2015) 14506–14513.

[13] J. van der Merwe, K. Uren, G. van Schoor, D. Bessarabov, Characterisation tools development for PEM electrolysers, Int. J. Hydrogen Energy 39 (26) (2014) 14212–14221.

[14] S. Ma, K. Wang, F. Xiao, T. Zhang, F. Ye, C. Xu, et al., In-plane performance analysis of PEM electrolyzer cell under multiple operating conditions based on anode segmented visualization design, Appl. Energy 381 (2025) 125167.

[15] I. Dedigama, P. Angeli, N. van Dijk, J. Millichamp, D. Tsaoulidis, P.R. Shearing, et al., Current density mapping and optical flow visualisation of a polymer electrolyte membrane water electrolyser, J. Power Sources 265 (2014) 97–103.

[16] N. Hensle, S. Metz, A. Weber, T. Smolinka, A segmented along the channel test cell for locally resolved analysis at high current densities in PEM water electrolysis, J. Electrochem. Soc. 171 (11) (2024) 114510.

[17] J.K. Lee, C. Lee, K.F. Fahy, B. Zhao, J.M. LaManna, E. Baltic, et al., Critical current density as a performance indicator for gas-evolving electrochemical devices, Cell Rep. Phys. Sci. 2 (5) (2021) 100440.

[18] Thomassen, et al., Method for Producing Hydrogen in a PEM Water Electrolyser System, PEM Water Electrolyser Cell, Stack and System, 2022. US 11,408,081 B2.

[19] M.R. Gerhardt, J.S. Østenstad, A.O. Barnett, M.S. Thomassen, Modeling contact resistance and water transport within a cathode liquid-fed proton exchange membrane electrolyzer, J. Electrochem. Soc. 170 (12) (2023) 124516.

[20] A. Tugirumubano, H.-J. Shin, S.-H. Go, M.-S. Lee, L.K. Kwac, H.-G. Kim, Electrochemical performance analysis of a PEM water electrolysis with cathode feed mode based on flow passage shape of titanium plates, Int. J. Precis. Eng. Manuf. 17 (8) (2016) 1073–1078.

[21] S. Toghyani, E. Afshari, E. Baniasadi, S.A. Atyabi, G.F. Naterer, Thermal and electrochemical performance assessment of a high temperature PEM electrolyzer, Energy 152 (2018) 237–246.

[22] E.A. Norman, V.M. Maestre, A. Ortiz, I. Ortiz, Steam electrolysis for green hydrogen generation. State of the art and research perspective, Renew. Sustain. Energy Rev. 202 (2024) 114725.

[23] S.D. Greenway, E.B. Fox, A.A. Ekechukwu, Proton exchange membrane (PEM) electrolyzer operation under anode liquid and cathode vapor feed configurations, Int. J. Hydrogen Energy 34 (16) (2009) 6603–6608.

[24] Tom Smolinka, What do we Need in PEM Water Electrolysis to Achieve our 2030 Targets: a Review of Key Challenges, 2023. Berlin.

[25] R. Lin, Y. Lu, J. Xu, J. Huo, X. Cai, Investigation on performance of proton exchange membrane electrolyzer with different flow field structures, Appl. Energy 326 (2022) 120011.

[26] M. Schönleber, D. Klotz, E. Ivers-Tiffée, A method for improving the robustness of linear kramers-kronig validity tests, Electrochim. Acta 131 (2014) 20–27.

[27] B.A. Boukamp, A linear kronig-kramers transform test for immittance data validation, J. Electrochem. Soc. 142 (6) (1995) 1885–1894.

[28] Q. Zhang, D. Wang, E. Schaltz, D.-I. Stroe, A. Gismero, B. Yang, Degradation mechanism analysis and state-of-health estimation for lithium-ion batteries based on distribution of relaxation times, J. Energy Storage 55 (2022) 105386.

[29] A. Weiß, S. Schindler, S. Galbiati, M.A. Danzer, R. Zeis, Distribution of relaxation times analysis of high-temperature PEM fuel cell impedance spectra, 0013-4686 230 (2017) 391–398.

[30] Batalla B. Sánchez, J. Bachmann, C. Weidlich, 0013-4686, Investigation of the Degradation of Proton Exchange Membrane Water Electrolysis Cells Using Electrochemical Impedance Spectroscopy with Distribution of Relaxation Times Analysis, 473, 2024 143492.

[31] H. Schichlein, A.C. Müller, M. Voigts, A. Krügel, E. Ivers-Tiffée, Deconvolution of electrochemical impedance spectra for the identification of electrode reaction mechanisms in solid oxide fuel cells, J. Appl. Electrochem. 32 (8) (2002) 875–882.

[32] S. Dierickx, A. Weber, E. Ivers-Tiffée, 0013-4686, How the Distribution of Relaxation Times Enhances Complex Equivalent Circuit Models for Fuel Cells, 355, 2020 136764.

[33] A.-L. Chan, H. Yu, K.S. Reeves, S.M. Alia, 0378-7753, Identifying Electrochemical Processes by Distribution of Relaxation Times in Proton Exchange Membrane Electrolyzers, 628, 2025 235850.

[34] D. Klotz, J.P. Schmidt, A. Kromp, A. Weber, E. Ivers-Tiffée, The distribution of relaxation times as beneficial tool for equivalent circuit modeling of fuel cells and batteries, ECS Trans. 41 (28) (2012) 25–33.

[35] A.N. Tichonov, A. Gončarskij, V.V. Stepanov, A.G. Jagola (Eds.), Numerical Methods for the Solution of Ill-Posed Problems, Springer, Dordrecht, 1995.

[36] E. Ivers-Tiffée, A. Weber, Evaluation of electrochemical impedance spectra by the distribution of relaxation times, J. Ceram. Soc. Japn. 125 (4) (2017) 193–201.

[37] A. Leonide, V. Sonn, A. Weber, E. Ivers-Tiffée, Evaluation and modeling of the cell resistance in anode-supported solid oxide fuel cells, J. Electrochem. Soc. 155 (1) (2008) B36.

[38] N. Hensle, D. Brinker, S. Metz, T. Smolinka, A. Weber, On the role of inductive loops at low frequencies in PEM electrolysis, Electrochem. Commun. 155 (2023) 107585.

[39] Brinker D, Hensle N, La Horstmann de Viña, Irene Franzetti, Jerónimo Bühre LV, Andaluri UA, Menke C et al. ; 2024.

[40] A. Schiefer, M. Heinzmann, A. Weber, Inductive low-frequency processes in PEMFC-impedance spectra, Fuel Cells 20 (4) (2020) 499–506.

[41] A. Roy, F.H. Roenning, D.S. Aaron, F.-Y. Zhang, M.M. Mench, Combining distributed electrochemical measurements with a semi-empirical model to identify local variations in overpotentials for PEM water electrolyzers, J. Electrochem. Soc. 172 (1) (2025) 14509.

[42] I.V. Pushkareva, M.A. Solovyev, S.I. Butrim, M.V. Kozlova, D.A. Simkin, A. S. Pushkarev, On the operational conditions' effect on the performance of an anion exchange membrane water electrolyzer: electrochemical impedance spectroscopy study, Membranes 13 (2) (2023) 192.

[43] J.-H. Kim, C.-Y. Oh, K-R. Kim, J.-P. Lee, T.-J. Kim, Parameter identification of electrical equivalent circuits including mass transfer parameters for the selection of the operating frequencies of pulsed PEM water electrolysis, Energies 15 (24) (2022) 9303.

[44] Z. Kang, S.M. Alia, J.L. Young, G. Bender, Effects of various parameters of different porous transport layers in proton exchange membrane water electrolysis, Electrochim. Acta 354 (2020) 136641.

[45] S. Park, J.-W. Lee, B.N. Popov, A review of gas diffusion layer in PEM fuel cells: materials and designs, Int. J. Hydrogen Energy 37 (7) (2012) 5850–5865.

[46] D. Malevich, E. Halliop, B.A. Peppley, J.G. Pharoah, K. Karan, Investigation of charge-transfer and mass-transport resistances in PEMFCs with microporous layer using electrochemical impedance spectroscopy, J. Electrochem. Soc. 156 (2) (2009) B216.

[47] Zhong Di, R. Lin, Z. Jiang, Y. Zhu, D. Liu, X. Cai, et al., Low temperature durability and consistency analysis of proton exchange membrane fuel cell stack based on comprehensive characterizations, Appl. Energy 264 (2020) 114626.

[48] T.A. Zawodzinski, C. Derouin, S. Radzinski, R.J. Sherman, T. van Smith, T. E. Springer, et al., Water uptake by and transport through nafion® 117 membranes, J. Electrochem. Soc. 140 (4) (1993) 1041–1047.

[49] T.E. Springer, T.A. Zawodzinski, S. Gottesfeld, Polymer electrolyte fuel cell model, J. Electrochem. Soc. 138 (8) (1991) 2334–2342.

[50] G.W. Thomson, The antoine equation for vapor-pressure data, Chem. Rev. 38 (1) (1946) 1–39.

[51] H.-S. Shin, B.S. Oh, Water transport according to temperature and current in PEM water electrolyzer, Int. J. Hydrogen Energy 45 (1) (2020) 56–63.

[52] T. Berning, On the nature of electro-osmotic drag, Energies 13 (18) (2020) 4726.

[53] P. Majsztrik, A. Bocarsly, J. Benziger, Water permeation through nafion membranes: the role of water activity, J. Phys. Chem. B 112 (51) (2008) 16280–16289.

[54] S. Motupally, A.J. m Beker, J.W. Weidner, Diffusion of Water in Nafion 115 Membranes, 2000.

[55] Pierre Millet, PEM water electrolysis, in: Hydrogen Production, John Wiley & Sons, Ltd, 2015, pp. 63–116.